OXFORD

ORIGINAL ARTICLE

Neuromuscular junctions are pathological but not denervated in two mouse models of spinal bulbar muscular atrophy

Jessica E. Poort[1], Mary B. Rheuben[1], S. Marc Breedlove[1] and Cynthia L. Jordan[1,*]

[1]Neuroscience Program, Michigan State University, MI, USA

*To whom correspondence should be addressed at: Cynthia L. Jordan, Neuroscience Program, Michigan State University, 293 Farm Lane, East Lansing, MI 48824. Tel: +517-355-1722; Email: jordancy@msu.edu

Abstract

Spinal bulbar muscular atrophy (SBMA) is a progressive, late onset neuromuscular disease causing motor dysfunction in men. While the morphology of the neuromuscular junction (NMJ) is typically affected by neuromuscular disease, whether NMJs in SBMA are similarly affected by disease is not known. Such information will shed light on whether defective NMJs might contribute to the loss of motor function and represent a potential therapeutic target for treating symptoms of SBMA. To address this gap in information, the morphology of NMJs was examined in two mouse models of SBMA, a myogenic model that overexpresses wildtype androgen receptor (AR) exclusively in muscle fibres and a knockin (KI) model expressing a humanized mutant *AR* gene. The tripartite motor synapse consisting of motor nerve terminal, terminal Schwann cells (tSCs) and postsynaptic specialization were visualized and analysed using confocal microscopy. Counter to expectation, we found no evidence of denervation in either model, but junctions in both models show pathological fragmentation and an abnormal synaptophysin distribution consistent with functionally weak synapses. Neurofilament accumulations were observed only in the myogenic model, even though axonal transport dysfunction is characteristic of both models. The ultrastructure of NMJs revealed additional pathology, including deficits in docked vesicles presynaptically, wider synaptic clefts, and simpler secondary folds postsynaptically. The observed pathology of NMJs in diseased SBMA mice is likely the morphological correlates of defects in synaptic function which may underlie motor impairments associated with SBMA.

Introduction

Motoneuron disease is often characterized by a distal axonopathy, with neuromuscular junctions (NMJ) affected first, well before pathology in the motoneurons (1–7). Common markers of disease at the NMJ include loss of nerve terminals causing partial or complete denervation of the muscle fibre, junctional fragmentation, and neurofilament accumulation in the nerve terminal itself. Despite substantial precedent that the NMJ may be an early site of pathology for many motoneuron diseases, whether NMJs are affected in spinal bulbar muscular atrophy (SBMA) is largely unexplored.

SBMA is a progressive, late onset neuromuscular disease involving motoneuron loss, muscle weakness, and atrophy. Its known cause is an expansion of a CAG/glutamine repeat (polyQ) in the first exon of the *androgen receptor (AR)* gene (8). Recent evidence suggests that expression of the disease depends not only on having the mutant *AR* allele, but also on male levels of testosterone (T), possibly explaining why only males are clinically affected (9–11). The hallmark post-mortem pathology of SBMA is motoneuron loss in the anterior horn of the spinal cord and in brainstem motor nuclei, but skeletal muscles are also affected (12,13). Muscle biopsies reveal that affected muscles
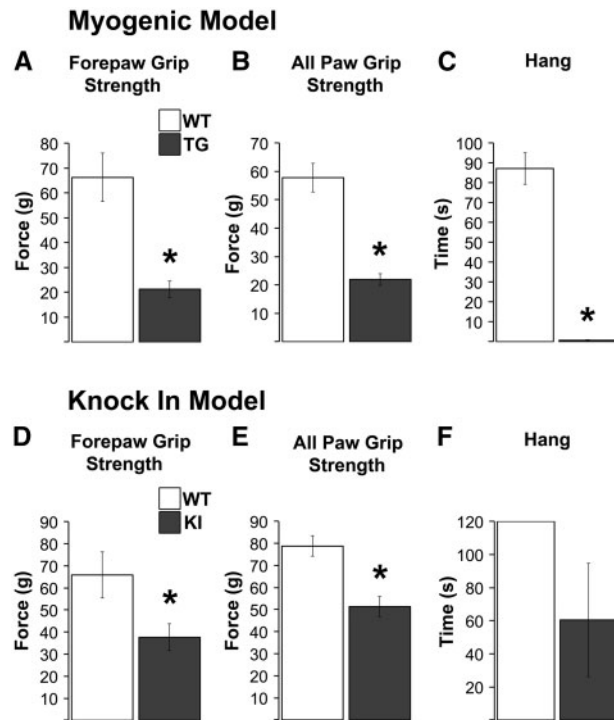
Figure 1. Male mice of two different SBMA models (myogenic transgenic (TG) and knock-in (KI)) show the expected motor impairments. Grip strength, based on measures of forepaws and all paws was significantly decreased in myogenic TG males compared to wildtype (WT) control males (**A, B**). TG males also showed profound deficits in mean hang time, another indicator of overall neuromuscular function (**C**). As expected, grip strength in KI males was not as severely impaired as TG males, but nonetheless showed significant deficits (**D, E**). KI hang times were reduced, but not significantly, likely due to the substantial variance in KI males (**F**). *$P < 0.05$ compared to WT controls. Error bars represent standard error of the mean, with $n = 8$ mice/group for TGs and 5 mice/group for KIs that contributed to the confocal analysis. The second cohort of TG and KI males used for the EM analysis showed comparable levels of dysfunction as shown here.

contain both atrophic and hypertrophic fibres suggestive of neurogenic causes, but fibres with internalized nuclei, angular and/or split fibres in muscle biopsies also suggest primary myogenic causes (13). Because both the motoneurons and their skeletal muscle targets are affected by disease, it seems likely that NMJs will be as well.

While denervation of the NMJ is perhaps the most obvious change during disease, *any* alteration at the junction, including the associated terminal Schwann cells (tSCs) that cap the junction, or the muscle endplate itself, have the potential of affecting synaptic function and thus motor function. For example, while junctions in models of spinal muscular atrophy (SMA), caused by a genetic defect in the *survival motor neuron one* (*SMN1*) gene, ultimately become denervated (14–16), earlier in the disease process junctions exhibit no signs of anatomical denervation but nonetheless show morphological and functional changes (1). Notably, these pathological changes at the NMJ were found to precede overt deficits in motor function, indicating that subtle changes in the junction prior to overt denervation are some of the earliest pathological events in SMA. Targeting such early events could potentially stop disease and preserve motor function before motoneurons and their peripheral connections are lost.

We examined the NMJs in two different SBMA mouse models. One model is a transgenic (TG) mouse in which wildtype rat

AR is expressed exclusively in skeletal muscle fibres and is referred to as the myogenic model of SBMA (17). The second model is a knock-in (KI) mouse in which the first exon in the endogenous *AR* gene is replaced by the first exon of the human *AR* gene harbouring 113 CAG repeats (6). Remarkably, despite the difference in how each model was engineered, both models display features characteristic of human SBMA, suggesting that both are valid models of this disease. For example, like SBMA in humans, only males, and not females carrying the disease allele, show symptoms of disease. Likewise, the disease phenotype is androgen-dependent, with symptoms reversed or prevented when the gonads are removed from male SBMA mice. Moreover, diseased males of both models show the expected histopathology in skeletal muscle, including evidence of atrophic fibres and internalized nuclei (6,9,17,18). Of note, neither model shows evidence of motoneuron cell death even after motor function is severely compromised, raising the question of what might trigger the loss of motor function in humans with SBMA. Recent results indicate that neuromuscular transmission is defective in both models (19). For example, activated nerve terminals in muscles from diseased myogenic and KI males release about one-third less neurotransmitter than normal. The current study is aimed at identifying the morphological substrates of these defects in function.

In this study, we examined the morphology of junctions in myogenic and KI males, comparing their junctions to those of age-matched wildtype (WT) controls generated in the same colony, often brothers of the diseased males within each model. Using both confocal and electron microscopy, we find striking pathology at the junction of SBMA mice, including evidence of both pre- and postsynaptic changes. Core features of pathology shared by both models include junctional fragmentation, a widened synaptic cleft, and simplified secondary postsynaptic folds. Not only are these data consistent with the idea that pathology at the NMJ may contribute to impaired motor function at the behavioral level, but also that AR acting in muscle fibres is an important source of toxicity triggering this pathology.

Results

SBMA models show the expected deficit in motor function

As expected, myogenic TG males show profound motor deficits in all measures (17,18). Both fore- and all-paw grip strength and hang tests reveal significant deficits when compared to WT controls (Figure 1A–C; P-values < 0.001 for all measures). Effects of disease on motor function in KI males are much milder. Nonetheless, significant deficits were apparent in both fore- and all-paw grip strength (Figure 1D and E, ps < 0.05). While a deficit in hang times was also found (Figure 1F), it was not significant, likely due to the marked increase in the variance of KI males on this measure. Since grip strength in this model was originally characterized based on a triangle bar rather than the grid (6), we also assessed grip strength using the triangle bar and confirmed the deficit previously reported based on this method ($84.4 \, g \pm 18.4 \, g$ for WT and $41.1 \, g \pm 1.6 \, g$ for KI, $P < 0.02$).

Disease does not induce denervation of NMJs in SBMA mice

Given the reported upregulated expression of molecular markers suggestive of denervation in diseased muscle of these
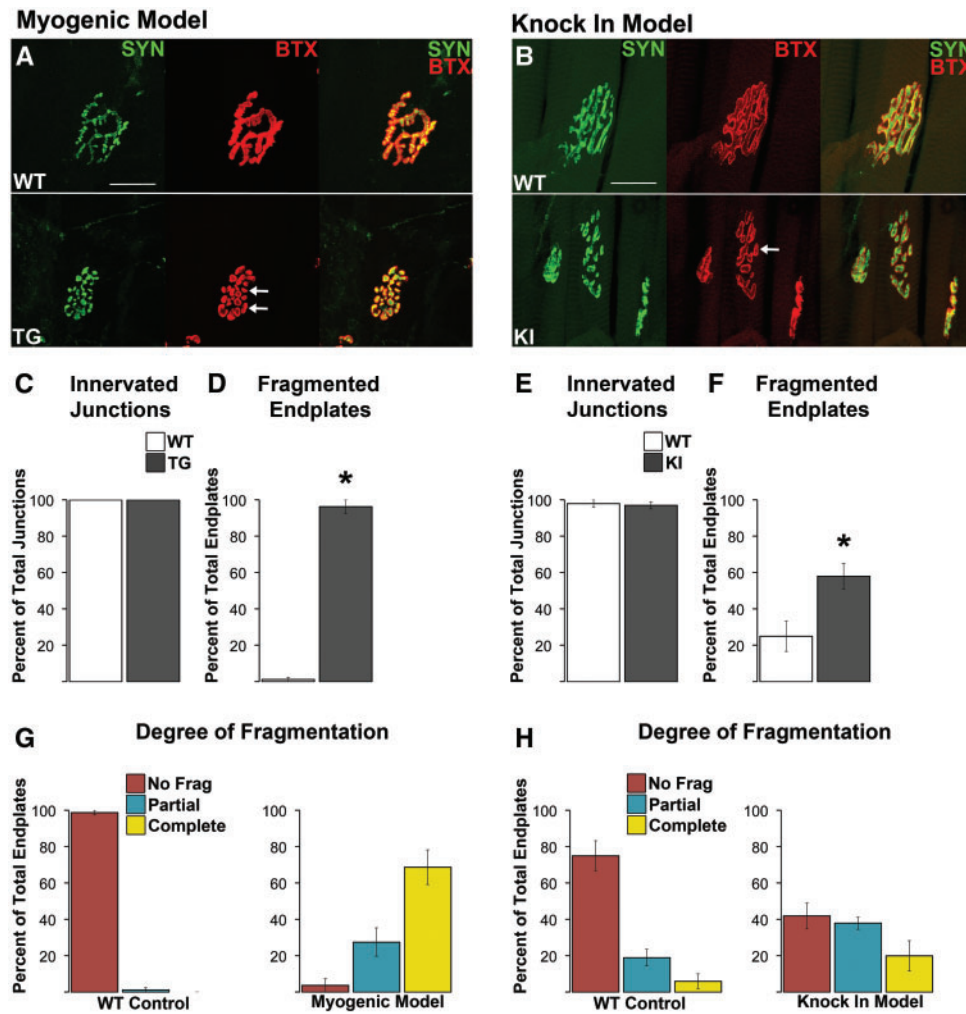
Figure 2. Neuromuscular junctions (NMJs) in both diseased TG and KI males show no evidence of morphological denervation but are consistently fragmented. Despite notable fragmentation, pre- and postsynaptic components of the NMJ showed precise alignment between the overlying synaptophysin labelled nerve terminals and the underlying α-bungarotoxin labelled (BTX) acetylcholine receptors (**A, B**). In short, there was no evidence of exposed endplates indicative of denervation (**B, F**). NMJs of wildtype (WT) muscle showed the typical, pretzel like morphology (**A**), albeit junctions in the levator ani (LA) muscle used for the KI model normally look more fragmented, like a collection of grapes. Regardless, using a consistent criterion to identify and count the number of distinct postsynaptic clusters that made up the junction revealed that junctions in diseased muscle of both TG (**A**) and KI males (**E**) are markedly fragmented (white arrows point to examples of) compared to WT junctions. Nearly every NMJ in the anterior tibialis of myogenic TG males (**C**) was fragmented while 58% of LA junctions in KI males show fragmentation (**G**). Assessing the degree of fragmentation within each NMJ revealed that nearly all myogenic junctions are completely fragmented (**D**), while only about 20% of KI junctions show complete fragmentation. * $P < 0.05$ compared to WT controls. Error bars represent standard error of the mean, with $n = 4$ mice/group for TG and $n = 5$ mice/group for KI estimates of denervation and fragmentation. Twenty junctions were examined per mouse. Scale bars indicate 25 microns.

two models (6,17), we initially looked for morphological evidence of denervation. NMJs were evaluated for evidence of denervation based on whether the endplate marked by AChR staining lacked, either fully or partially, an overlying nerve terminal, visualized with YFP (myogenic) and/or synaptophysin (myogenic and KI) staining. Regardless of the method used to visualize nerve terminals, junctions looked fully innervated in diseased muscle from the same male mice that showed robust defects in motor function (Figure 1). Indeed, nerve terminal branches aligned precisely with the postsynaptic specialization in both diseased and WT muscle (Figure 2A and B). Quantitative analysis confirmed our impression that disease does not cause endplates to become either partially or fully denervated for either myogenic or KI males (Figure 2C and E). Next we examined the NMJ for other signs of pathology that might account for the loss in synaptic function.

Diseased NMJS Are Fragmented

The conformation of the NMJ is markedly perturbed in muscles from diseased males of both SBMA models. While normal mammalian junctions typically have a continuous pretzel-like appearance, diseased junctions show a distinct fragmented appearance, consisting of many small punctate domains (Figure 2A and B). In the myogenic model, quantitative analyses of TA endplates show that few ($1.25\% \pm 1.25$) WT junctions are fragmented whereas virtually all endplates ($96.25\% \pm 3.75\%$, Figure 2D, $P < 0.05$) show some degree of fragmentation in diseased TG males. Furthermore, around 70% of TG endplates are extremely fragmented with fewer than 30% showing partial fragmentation (Figure 2G). While NMJs in affected KI males are also fragmented (Figure 2B), the phenotype in this model is less severe, with about 60% overall showing some degree of fragmentation, with the majority being partially fragmented (Figure 2F and H).

Table 1. Electron microscopic measures of presynaptic features of diseased and healthy neuromuscular junctions in two SBMA mouse models, the TG myogenic model and the KI model. Values shown are mean ± SEM of 10 junctions from each of 3 mice/group. Statistically significant values denoted in bold font.

measure	Myogenic (TG) model Genotype		P value	Knockin (KI) model Genotype		P value
	WT	TG	P	WT	KI	p
Terminal Profile Cross Section Area (μm^2)	3.05 ±0.34	3.91 ±0.53	0.174	3.20 ±0.38	2.89 ±0.33	0.541
Vesicle Density (Vesicles/μm^2 of terminal profile)	58.19 ±4.16	48.97 ±3.6	0.100	63.26 ±8.26	60.04 ±3.92	0.726
Readily Releasable Vesicle Density (Vesicles/μm^2 in appositional band/terminal profile)	101.33 ±5.66	97.9 ±6.64	0.696	93.98 ±6.73	94.21 ±5.17	0.978
Mitochondrial Cross Sectional Area	**0.48 ±0.08**	**1.01 ±0.16**	**0.004**	**0.58 ±0.10**	**0.35 ±0.05**	**0.054**
Number of Mitochondria (Per terminal profile)	7.97 ±1.22	10.33 ±1.27	0.180	9.07 ±1.38	7.1 ±1.03	0.259
Number of Active Zones (Per μm of apposition length)	0.62 ±0.07	0.59 ±0.06	0.791	0.33 ±0.06	0.33 ±0.07	0.786
Number of Active Zones Without Docked Vesicles (Empty AZ/Total)	**0.32 ±0.07**	**0.53 ±0.07**	**0.037**	0.29 ±0.07	0.26 ±0.07	0.789
Vesicle Shape (Aspect Ratio)	**1.17 ±0.01**	**1.22 ±0.01**	**0.001**	**1.2 ±0.01**	**1.23 ±0.01**	**0.024**
Vesicle Diameter (nm)	24.39 ±0.51	23.92 ±0.23	0.416	24.25 ±0.4	24.07 ±0.19	0.684

Although LA junctions in WT muscle have a normal tendency to be fragmented (∼25%), much more so than TA junctions (Supplementary Material, Table 1), disease nonetheless increased significantly the amount of fragmentation seen (Figure 1F, $P < 0.05$), indicating its pathological nature. In sum, disease in *both* models is associated with fragmentation of the NMJ, despite expressing quite different disease alleles. These data prompt the question of whether the fragmentation of junctions also occurs in men affected by SBMA and play a role in the neuromuscular dysfunction associated with this disease.

Disease Decreases the Size of Muscle Fibres in Both Models But Endplate size Only in the Myogenic Model

We find that the size of both TA muscle fibres and their endplates in myogenic males is significantly decreased compared to WTs (Figure 3A and B, ps < 0.035). While disease also significantly decreased the size of LA fibres in KI males (Figure 3C, $P = 0.003$), as previously shown (6), the size of LA endplates is unchanged (Figure 3D).

## Disease Leads to Abnormal Synaptophysin Staining

We previously showed that both models show defects in the retrograde transport of endosomes, which likely originates in the motor nerve terminal (20). Additionally, synaptophysin accumulations in perijunctional, preterminal axons have been reported in another TG mouse model of SBMA (7). These observations prompted us to examine the distribution of synaptophysin in the nerve terminal and its preterminal axon. We find that synaptophysin staining is enhanced in nerve terminals of diseased myogenic TG males compared to WT controls. When such staining was quantified, values indicate that the proportion of endplate covered by synaptophysin (i.e., "synaptophysin coverage") is increased in TGs compared to WTs (Figure 4A and D), although this difference fell short of

significance. We also find that 35% of junctions in diseased TG myogenic males contain synaptophysin in the preterminal axon (unmyelinated portion of the motor axon just proximal to the terminal) compared to only ∼1% of junctions in WT males (Figure 4A and E, $P = 0.004$). This unusual pattern of synaptophysin labelling is consistent with the impairments seen in retrograde axonal transport in this same model. Although we find none of the abnormal synaptophysin staining in LA junctions of KI males, we did find comparable synaptophysin pathology in motor nerve terminals of TA muscle of KI males, with an increase in the amount of endplate area covered by synaptophysin once images were thresholded (Supplementary Material, Table 1), consistent with the transport dysfunction reported for this model (20).

Disease Causes Neurofilament Accumulations Only in the Myogenic Model

A factor potentially affecting endosomal movement is the condition of the neurofilament proteins in the cytoskeleton. Indeed, we find substantial evidence for neurofilament accumulations in both nerve terminals and preterminal axons in muscle of diseased myogenic males (Figure 4B and C). Large, bulbous enlargements of neurofilament protein were rare in WT motor axons connected to *en face* junctions, but over 50% of such motor axons in diseased myogenic muscle contained neurofilament accumulations (Figure 4F, $P < 0.05$). Similarly, over 40% of nerve terminals in diseased muscle contain neurofilament accumulations compared to only ∼8% of WT nerve terminals (Figure 4G, $P = 0.005$). However, we find no evidence of neurofilament accumulations in the LA muscle of diseased KI males, in either the nerve terminals or motor axons. To explore whether differences in muscle might explain the lack of such pathology in the KI model, we also examined the TA in KI males but found no evidence of neurofilament accumulations there either (Supplementary Material, Table 1). Hence, it is unlikely that

Myogenic Model

Knock In Model
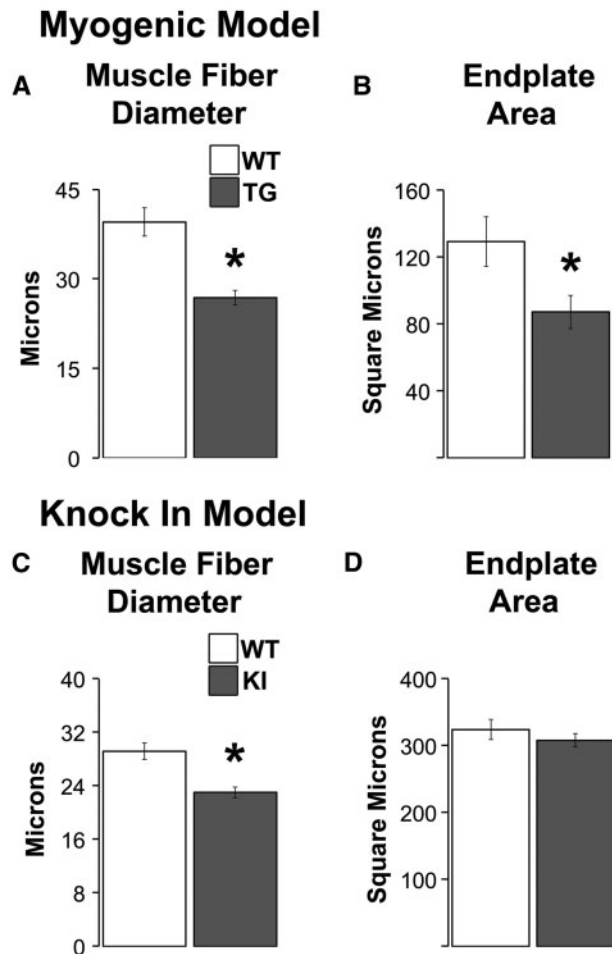
Figure 3. Endplates are reduced in size only in myogenic TG males but muscle fibres are smaller in diseased males of both models. The size of both fibres and endplates are significantly reduced in TG myogenic males compared to WT males (**A, B**). While muscle fibres are also smaller in diseased KI males compared to healthy WTs (**C**), the size of endplates is unaffected by disease in this model (**D**). This dissociation between endplate and fibre size in diseased KI males raises the possibility that synaptic strength is spared in KI males but direct measures of synaptic strength indicate the opposite, with significant losses in strength in both models (19). * $P < 0.05$ compared to WT controls. Error bars represent standard error of the mean. n = 4–5 mice/group for estimates of fibre diameter and n = 5–7 mice/group for estimates of endplate area. Twenty junctions were sampled per muscle/animal.

neurofilament accumulations underlie the defects in retrograde transport found in this model (20). Moreover, finding that the pattern of neurofilament and synaptophysin staining in the presynapse is altered in the myogenic model in which the disease allele is expressed *only* postsynaptically demonstrates how pathological processes in muscle fibres can induce pathology in the motor nerve terminals and presumably, in the motoneurons themselves.

### tSC morphology was negligibly affected by disease

Our confocal analysis of tSCs in the S100/AChR stained series revealed subtle changes in their morphology but only in the myogenic model. While the frequency of tSC sprouting appeared to be increased by disease in myogenic muscle (0.10 ± 0.03% of WT junctions versus 0.22 ± 0.06% TG junctions), this increase was not significant ($P = 0.144$). Note that tSC

sprouting was a rare event regardless of genotype. Also, the number of tSCs was significantly decreased by disease in the myogenic model (2.75 ± 0.03 in WT versus 2.13 + 0.10 in TG, $P = 0.005$). This effect was not unexpected, since junctions in TG muscle are significantly smaller than normal and the number of tSCs per junction tends to correlate with junctional size (21). This relationship predicts that if junctional size is taken into account, the difference in number would be eliminated as indeed occurred (2.20 + 0.709 × 10^{-2} in TG versus 1.24 + 0.356 × 10^{-2} in WT, $P = 0.400$). The heavy investment of connective tissue in the LA interfered with S100 staining in this muscle, limiting our analysis of tSCs in the KI model to the TA where we found no effects of disease. A caveat of the TA is that the low level of ARs in this muscle means that it is considerably less affected than the LA.

Disease Affects the Ultrastructure of Nerve Terminals Primarily in the Myogenic Model

Our confocal results prompted questions about potential pathology of NMJs at the ultrastructural level. In particular, whether the abnormal pattern of synaptophysin staining reflects changes in the distribution of synaptic vesicles, which could only be assessed at the EM level. Qualitatively, terminal profiles in both models look normal, with neither model showing obvious evidence of neurofilament accumulations, altered distribution of vesicles, or abnormal features of internal structures, such as unusual mitochondrial cristae. That we did not find evidence of neurofilament accumulations in nerve terminals of myogenic junctions was unexpected, given our confocal findings. Because muscles came from appreciably younger but comparably impaired myogenic mice for the EM analysis, it is possible that such accumulations develop at a later stage and are indicative of late-stage disease. Indeed, this is consistent with the lack of neurofilament accumulations in KI males that rarely reach late-stage disease (19) due to toxic uraemia, which causes many to die before marked motor dysfunction emerges (6). Moreover, quantitative measurements indicated no differences between WT and diseased nerve terminals in terminal profile size, overall vesicle density, or the density of vesicles in the readily releasable pool (RRP; Table 1). As expected, the vesicle density in the RRP (measured for this purpose as a 480 nm strip of terminal immediately across from the secondary clefts) was about twice as dense as overall. Despite the generally normal appearance of the junctions, several pathological features stood out. For example, in the myogenic model, the size of mitochondria was increased in diseased nerve terminals compared to WT controls (Figure 5A and B, $P = 0.004$) although comparable pathology was not detected in the KI model (Table 1). While disease also increased the number of mitochondria in the myogenic model by ~25%, this effect was not significant (Table 1). However, neither the size nor number of mitochondria was affected in diseased KI males (Table 1).

While the number of active zones per terminal apposition length was not affected by disease in either model (Table 1), the density of vesicles docked at active zones in myogenic males was, with significantly fewer docked vesicles at active zones compared to WT controls (Figure 5D, $P = 0.032$). Consequently, the proportion of active zones without docked vesicles was significantly increased by disease (Figure 5E, $P = 0.037$). However, we find no such effects of disease in the KI model, on either the overall number of docked vesicles or the number of active zones containing docked vesicles (Table 1). This may reflect the fact
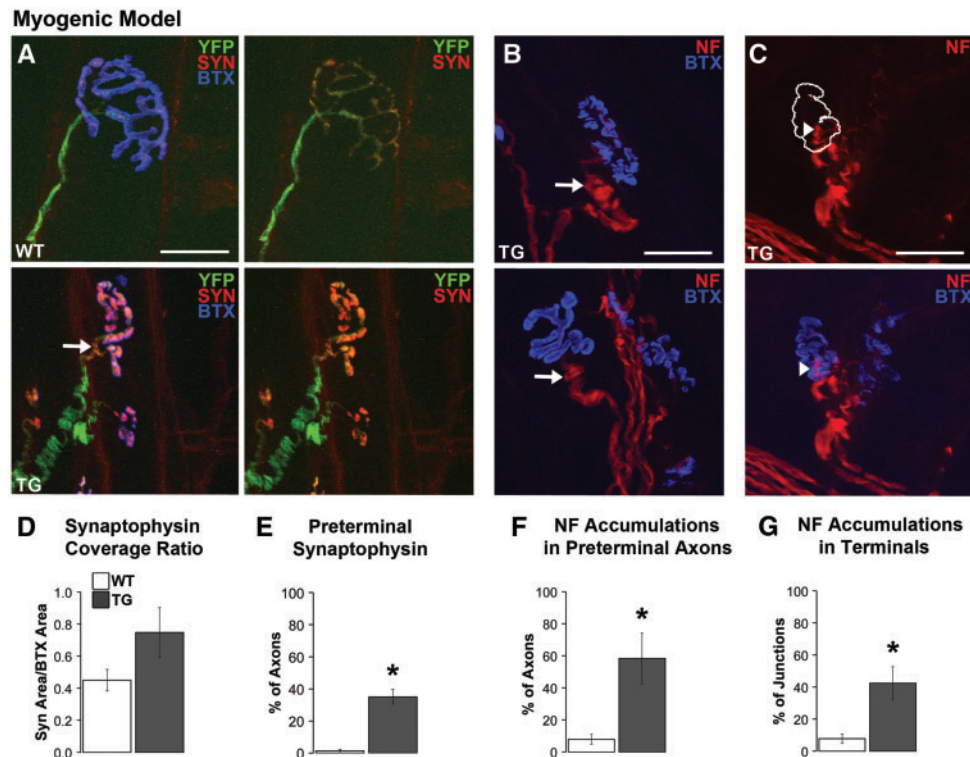
Figure 4. Disease alters the distribution of synaptophysin (SYN) and triggers neurofilament (NF) accumulations in preterminal axons and nerve terminals of myogenic males. Synaptophysin staining was sparse in WT nerve terminals compared to a notable increased density within the nerve terminals of TG males (**A**). As a result, a greater percentage of the endplate was covered by synaptophysin staining in TG nerve terminals compared to WT terminals (**D**). Moreover, synaptophysin staining extended into the preterminal axon (by about 5 μm, arrow in A) in nearly 40% of TG junctions (**E**) compared to little or no such staining in preterminal axons of WT junctions. NF accumulations, which appeared as localized NF-positive bulbous swellings (>2 times of the overall calibre of the axon) in the preterminal unmyelinated axon (**B**, arrows) and nerve terminal (**C**, arrowhead) of diseased muscle from TG males. Such NF accumulations were often associated with a marked increase in staining intensity. The white outline in C denotes where the postsynaptic BTX label is found (shown in the image below). NF accumulations in the preterminal axon are also prominent at this junction (**C**). Forty to sixty percent of junctions contained NF accumulations in either presynaptic axons (**F**) and/or in the terminal itself (**G**). * $P < 0.05$ compared to WT controls. Error bars represent standard error of the mean, with $n = 6$–7 mice/group for synaptophysin estimates and 4–5 mice/group for neurofilament measures, with 20 junctions measured per mouse. Scale bars represent 25 μm.

that KI males are at an earlier stage of disease than myogenic males (19).

We did find disease-related changes in the shape of vesicles in both SBMA models. To evaluate the shape of vesicles, we measured the length of each vesicular axis in the RRP to create an aspect ratio, which provides information on the roundness of each vesicle. We find that vesicles in both the TG and KI models are less round than those in matched WT controls (Figure 5F and H, $P < 0.01$ and $P = 0.024$, respectively). While there was no difference in mean vesicular diameter in either model (Table 1), the distribution of vesicle sizes (based on average diameter) appeared somewhat narrower, centreing more around the mean in diseased versus controls in both models, although these apparent differences were not significant (Figure 5G and I).

Disease Comparably Affects the Primary Cleft in Both Models

A factor that could reduce synaptic signalling to the muscle is increasing the distance acetylcholine must travel before reaching its receptors on the muscle surface. Measuring the distance (demarcated by thick lines in Figure 6A) from the outer plasma membrane of the nerve terminal to the top of each postsynaptic fold, where AChRs are located, revealed that it is significantly

increased by disease in both models (Figure 6A – D; $P = 0.040$ and 0.001 for TG and KI models, respectively). The increased width of the primary cleft in diseased junctions meant that the total cross sectional area of the primary cleft was also significantly increased (Table 2).

Disease Affects the Ultrastructure of the Postsynaptic Specialization Primarily in the KI Model

Models of neuromuscular disease often show a simplification of the postsynaptic folds that constitute the secondary clefts, manifesting as shallower clefts, with wider mouths (1,22,23). We find similar changes in the junctions of KI males. Whereas the secondary clefts of WT junctions are closely spaced, long, and thin, the secondary clefts of KI junctions are spaced farther apart, have wider mouths, and span a larger area (Figure 6E). However, our quantitative analysis also revealed that junctions in diseased KI males have a greater postsynaptic perimeter (relative to apposition length) compared to WT junctions (Figure 6F, $P = 0.01$). To understand what might account for this increased perimeter, we counted the number of terminations per secondary cleft as an indication of secondary fold complexity and find a significant increase in this measure at KI junctions compared to WT controls (1.44 ± 0.05 terminations per cleft per KI junction versus 1.19 ± 0.03 terminations per WT junction, $P < 0.000$). While the number of secondary clefts
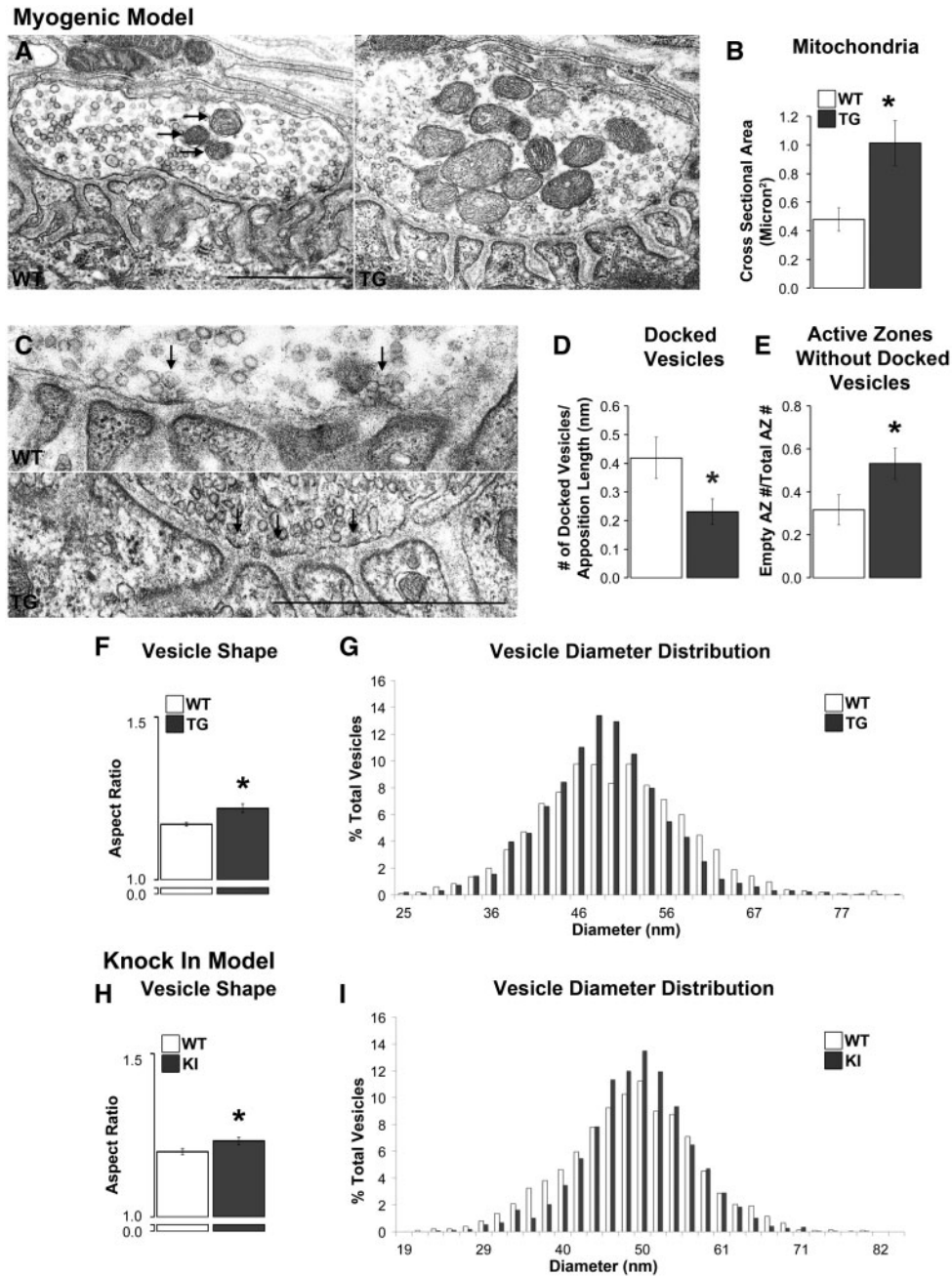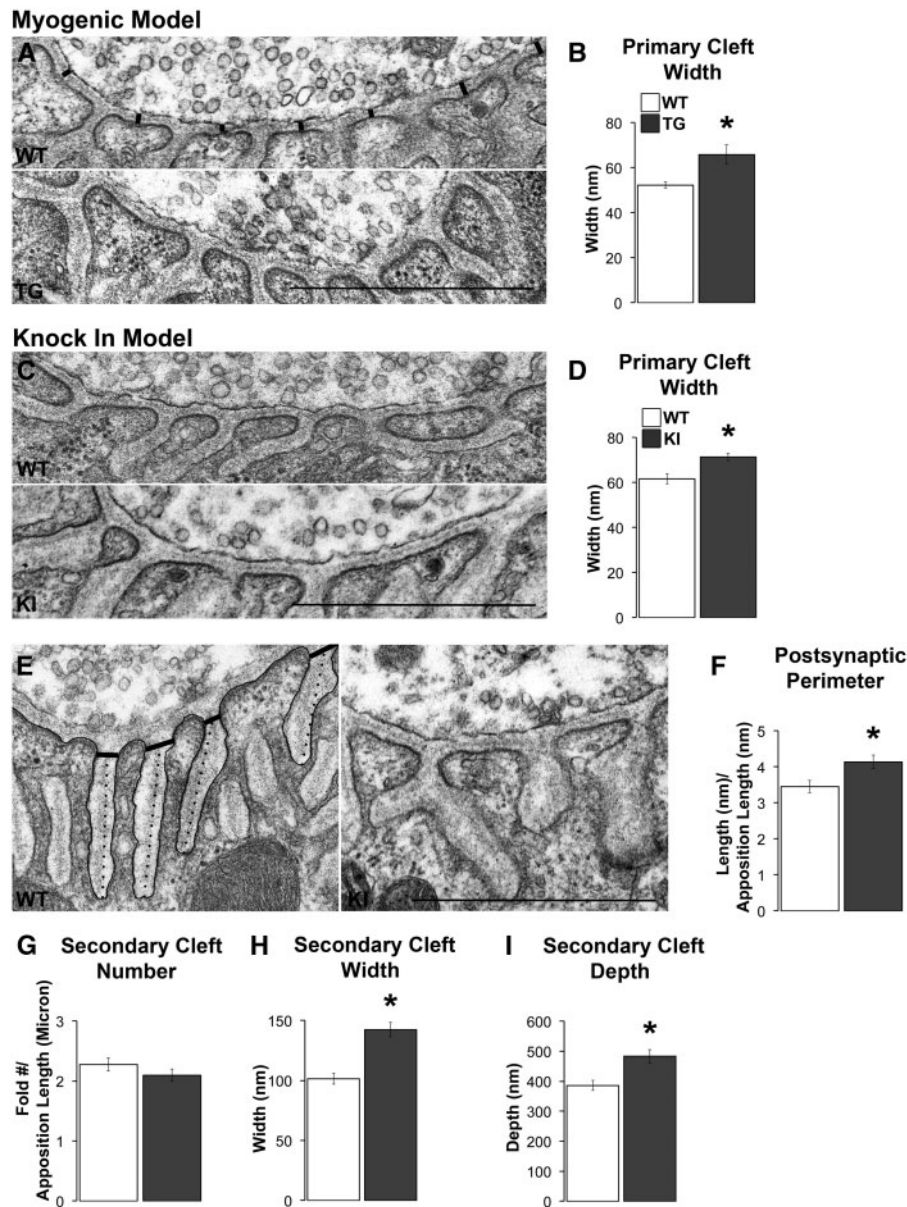
Figure 5. Disease affects the ultrastructure of motor nerve terminals primarily in myogenic TG males. The cross sectional area of mitochondria (arrows) in TG nerve terminals was significantly larger than in WT terminals (**A, B**) despite no changes in their number. While the number of active zones, which were identified by an electron dense area directly across from the mouth of a postsynaptic fold (**C**, denoted with arrows), per length of nerve terminal was unaffected by disease (Table 1), the number of docked vesicles contacting presynaptic membrane per active zone was, with significantly fewer docked vesicles at active zones in TGs compared to WTs (**D**). Consistent with this finding, the number of active zones without docked vesicles was *increased* in TG terminals compared to WT terminals (**E**). Vesicles in TG nerve terminals were also less round than WT vesicles based on their aspect ratio (minimum diameter over maximum diameter; **F**) although the distribution of average vesicle diameters appeared narrower and more centred around the mean in TG than WT terminals (**G**). Nerve terminals in KI compared to WT males showed less effects of disease with no difference in the number of active zones, docked vesicles, or active zones without docked vesicles (Table 1). However, vesicles in KI nerve terminals show an increase in their aspect ratio, like TG males, indicating that they are less round than those in WT males (**H**). Likewise, the distribution of vesicle diameters was narrower and more centred around the mean (**I**). * $P < 0.05$ compared to WT controls. Error bars represent standard error of the mean, with $n = 30$ junctions/group sampled from 3 animals/group, with 10 junctions sampled from each animal. Scale bars represent 1 µm.

did not differ between KIs and WTs, both the width at the mouth of the fold (indicated by the transverse lines in Figure 6E) and the depth of the cleft (indicated by dotted lines in Figure 6E) were significantly increased in KI males (Figure 6H and I, ps < 0.001). While measures of the secondary clefts in diseased myogenic males indicated that they also tend to be wider, but with shallower clefts and fewer terminal branches, amounting to a decrease in the total postsynaptic perimeter (4.74 ± 0.26 µm in WT versus 4.00 ± 0.32 µm in TG; normalized to apposition length), none of these changes were significant (Table 2).

Figure 6. Disease affects the ultrastructure of postsynaptic junctions primarily in symptomatic KI males. Although the synaptic cleft in WT muscle showed tight apposition between the pre- and postsynaptic specializations, the synaptic cleft of diseased junctions appeared much looser (**A, C**). When measured (A, black lines), the width of the primary cleft was increased in both models (**B, D**). The postsynaptic folds of KI junctions also appeared simplified (**E**), a phenomenon not seen in TG junctions. The postsynaptic perimeter, indicated by the black tracing, was increased in KI junctions compared to WT junctions (**F**). While the number of secondary clefts for KI junctions did not appear appreciably affected by disease (**G**), the width of secondary clefts, measured at a standard distance from the cleft opening (denoted by the thick black lines in E), was increased in KI junctions compared to WT junctions (**H**). The depth of the secondary cleft of KI junctions was also increased (**I**), measured as indicated by the dotted lines in E. * $P < 0.05$ compared to WT. Error bars represent standard error of the mean, with N = 30 junctions/group, with 3 animals/group, and 10 junctions sampled from each animal. Scale bars represent one micron.

Discussion

The effects of disease on the morphology of NMJs in SBMA mouse models had not been examined, despite considerable precedent in models of other motoneuron diseases that junctions are not only vulnerable to disease, but junctional pathology is one of the earliest signs of disease (1–7). Thus, we examined NMJs using both confocal and electron microscopy in chronically diseased males of two mouse models of SBMA, a muscle-specific TG model in which a wildtype allele of *AR* is overexpressed exclusively in muscle fibres (referred to as the myogenic TG model) and a KI model expressing the endogenous mouse *AR* gene containing the first exon of the human *AR* gene harbouring a disease-causing CAG expansion (6,17). Significantly, we find that neither model shows overt signs of denervation, although NMJs in both models are strikingly fragmented, a common outcome of motoneuron disease. Interestingly, junctional fragmentation is also characteristic of NMJs in models of muscular dystrophy (23–27), an exclusively muscle-driven disease. While the ultrastructure of the NMJ is affected in both SBMA models, the disease is expressed primarily on the presynaptic side in the myogenic model while expressed primarily on the postsynaptic side in the KI model. Our findings

Table 2. Electron microscopic measures of postsynaptic features of diseased and healthy neuromuscular junctions in two SBMA mouse models, the TG myogenic model and the KI model. Unexpectedly, disease predominantly affects postsynaptic features in KI mice and not in myogenic mice where expression of the disease allele is only in muscle fibres. Values shown are mean ± SEM of 10 junctions from each of 3 mice/group. Statistically significant values denoted in bold font.

measure	Myogenic (TG) model		P value	Knockin (KI) model		P value
	Genotype			Genotype		
	WT	TG	P	WT	KI	p
Primary Synaptic Cleft Area, μm^2 (Per μm of apposition length)	**51.66** ±1.54	**71.28** ±9.61	**0.049**	**57.4** ±2.12	**65.79** ±1.48	**0.002**
Secondary Cleft Number (Per μm of apposition length)	2.62 ±0.14	2.23 ±0.25	0.169	2.27 ±0.11	2.09 ±0.10	0.232
Number of Secondary Cleft Terminations (Per Cleft)	1.29 ±0.04	1.27 ±0.05	0.690	**1.19** ±0.03	**1.44** ±0.05	**0.000**
Synaptic Cleft Depth, nm^2	485.59 ±18.78	468.88 ±30.59	0.644	**385.44** ±16.74	**483.65** ±22.12	**0.001**
Secondary Cleft Width, nm^2	94.23 ±4.56	104.73 ±5.76	0.158	**101.43** ±4.46	**142.34** ±5.99	**0.000**
Secondary Cleft Area, nm^2	676.55×10^2 ±43.60×10^2	793.73×10^2 ±78.99×10^2	0.199	**529.94×10^2** ±**27.19×10^2**	**1142.56×10^2** ±**77.15×10^2**	**0.000**
Postsynaptic Perimeter Length, μm (Per μm of apposition length)	4.74 ±0.26	4.00 ±0.32	0.080	**3.45** ±0.17	**4.14** ±0.19	**0.010**

support the idea that SBMA is neither a disease of just motoneurons nor just muscle, but rather a neuromuscular disease involving defects in both cellular partners through a complex and reciprocal interplay of disease signals that can originate first in muscle. NMJs, as the point of contact between motoneurons and muscles, are likely a critical site for the bi-directional exchange of disease-related signals.

NMJs of chronically diseased myogenic and KI males are not denervated

That NMJs in muscles from diseased males of either model did not show any evidence of denervation is counter to other findings from these same models suggesting the opposite. Males from both models show impairments in motor function, having atrophic muscles that show changes in gene expression suggestive of denervation (6,17). However, every diseased endplate in both models had an overlying nerve terminal precisely aligned with underlying AChRs with no part of the endplate exposed, which is typical of normal NMJs. Neither did we see evidence of denervation at the ultrastructural level. In short, loss of motor function in SBMA is probably not caused by morphological denervation of muscle endplates, not even partial denervation.

Our results do not, however, rule out the possibility that disease causes muscles to become *functionally* denervated, meaning that while nerve terminals are physically intact, they lose their ability to reliably elicit fibre contractions. This scenario could explain why diseased muscles show some characteristics of denervation, such as angular atrophic fibres, elevated levels of AChR α mRNA, and enhanced spontaneous activity, despite the apparent lack of morphological denervation. But even functional denervation in the form of chronic subthreshold or silent synapses seems unlikely since we see none of the morphological indicators typically associated with synaptic inactivity such as increased expression of extrajunctional AChR and sprouting of nerve terminals and/or tSCs (28–32). Nonetheless, the observed pathology in the current study is consistent with defects in synaptic function, as indeed physiological measures indicate (19). It may be that some correlates of denervation

are induced by pathological signals that are independent of activity.

NMJs of chronically diseased myogenic and KI males are fragmented

We find striking fragmentation of diseased junctions in the muscles of both models, comparable to previous reports of other mouse models of neuromuscular disease and aging (22,33–38). Notably, this same sort of fragmented junctional pathology, with precise matching of pre- and post-synaptic elements, is also prominent in models of muscular dystrophy (24–26,36), a myogenic disease. Given that the disease allele acts solely on muscle in the myogenic model, it is likely that such junctional fragmentation in both models is triggered by the action of the disease allele in skeletal muscle. Such pathology induced by muscle in motor nerve terminals underscores the profound influence diseased muscles can have on the motoneurons that innervate them, an idea reinforced by findings in a second muscle-specific model of SBMA (39). It is important to note that while clusters of AChRs in the endplate are disconnected and separate, the overlying bouton-like structures of nerve terminal are interconnected via fine processes that appear to lack the synaptic machinery necessary to be functional (data not shown).

What causes the shift from the normal pretzel-like appearance to apparently separate domains is under active study. Mechanisms of aging may be involved (38,40). When agrin, a motoneuron-derived proteoglycan that stabilizes the junction, undergoes enhanced cleavage, endplates become notably fragmented, as occurs in aging (37,40). Of note, even though agrin and neurotrypsin, the protease that cleaves agrin, are both expressed in motoneurons, the effect of this enhanced cleavage is realized at the level of the muscle fibre basal lamina, where intact agrin normally inhibits the dispersal of AChRs. Moreover, neuregulin1 overexpressed in motor axons also induces fragmented junctions, involving a signalling pathway mediated by the tSCs that cap the NMJ (41). These observations together underscore the important role that non-cell autonomous

mechanisms play in shaping the morphology and function of the neuromuscular synapse, presumably in both health and disease.

In models of muscular dystrophy, junctional fragmentation has historically been attributed to the ongoing degeneration and regeneration of muscle fibres, through which the shape of the synapse changes, an effect recapitulated experimentally (38). However, recent evidence shows that truncated dystrophins expressed only in muscle rescue muscles from degeneration but do not rescue junctions from fragmentation, showing that these two pathological processes depend on different mechanisms (24). Moreover, muscles of SBMA models typically show little to no overt muscle degeneration (6,17). It is also noteworthy that the same fragmented phenotype is seen when signalling via the neurotrophic receptor TrkB is blocked (37,42). Since expression of TrkB ligands is perturbed in the muscles of diseased SBMA mice (43,44), compromised neurotrophin signalling may also trigger fragmentation of NMJs.

While evidence suggests that tSCs critically mediate the formation of fragmented junctions by extending their processes into the primary cleft to wrap around and eventually engulf nerve terminals for their removal from the junction (41,45,46), our EM analysis did not reveal any signs of tSC invasions into the primary cleft. We did note however that the small interconnectives between bulbous contacts appeared fully ensheathed by tSCs. Such ensheathing did not align with postsynaptic densities or folds that would suggest this area was once functional. The chronic nature of the disease in both models however leaves open this possibility.

Because both models not only express their respective disease alleles from early in development, but it is also possible that some aspects of the normal maturation of NMJs were affected by the disease allele that might lead to fragmentation. Androgen during postnatal development can arrest the normal maturation of rat NMJs, by preventing normally occurring synapse elimination. The result is a persistent and stably maintained fragmented morphology (47,48). It is clear, however, that the development of NMJs in diseased muscle is normal in many ways, with well-developed postsynaptic folds and fibres that are singly, and not multiply, innervated. Because we find no evidence of junctional fragmentation in acutely diseased female myogenic mice (20), junctional fragmentation may reflect a response to earlier pathological events that ultimately contributes to the progressive weakening of neuromuscular synapses.

The synaptic cleft is wider in NMJs of chronically diseased myogenic and KI males

Another shared pathological trait was the significantly wider primary clefts, averaging 22% wider in myogenic junctions and 14% wider in KI junctions. A wider cleft requires released neurotransmitter to travel farther before binding to postsynaptic AChRs. Increases in the distance between the release and binding sites for neurotransmitter cause a slower rise to peak concentration of neurotransmitter at the postsynaptic receptors and a reduced peak concentration (49), potentially contributing to the weakening of synapses caused by disease in these models (19). Similar widening of the synaptic cleft in myasthenia gravis and muscular dystrophy models (50,51) is associated with decreases in synaptic strength (52,53). Other evidence suggests that a wider cleft also decreases the electrical resistance within the cleft, perturbing the optimal distance to maximize synaptic strength (54). Interestingly, both motoneurons and muscles

appear to have the capacity to actively regulate the width of the synaptic cleft to maximize synaptic strength, an ability that may be impaired in diseased junctions (54). Again, because the disease allele is expressed only in skeletal muscle fibres of the myogenic model, a defect in optimizing the width of the primary cleft to maximize synaptic strength may originate in the fibres in both models.

Compounding the potential deleterious effect of a widened primary cleft on synaptic strength is the decrease in docked vesicles at active zones of the nerve terminal, although this defect was evident only in the myogenic model. Interestingly, electrophysiological recordings of synaptic function indicate that diseased junctions in both models release less neurotransmitter when activated, but only the myogenic model shows a deficit in the size of the physiologically defined RRP (19) consistent with the morphological deficit we find here in the number of docked vesicles in this same model. The other main factor contributing to synaptic strength is the probability of vesicular release, which is perturbed in *both* models (19). In short, these data converge on the idea that vesicular trafficking is perturbed in the nerve terminal of diseased junctions, which leads to deficits in synaptic strength. This idea can be tested directly using live imaging approaches. Again, it is noteworthy that such deficits are likely driven by disease signals originating in muscle.

The disease was also associated with wider, deeper and more complex secondary clefts in the KI model (Table 2), with similar changes in the myogenic model. Such changes provide more membrane for AChRs at the crests of the fold and for sodium channels in the depths of the clefts (55) and may enhance the effect of released neurotransmitter by lowering the threshold for depolarization of the muscle fibre, as indeed we have found (19). This increased excitability of muscle fibres may be an attempt to compensate for the declining strength of nerve terminals (56). Because dystrophin promotes the development of the secondary folds (23,24,26,27,36), dystrophin-related mechanisms may be involved in the postsynaptic changes we see in SBMA mice. Critical mechanisms mediating hyperexcitability of skeletal muscles in myotonic dystrophy have also been implicated in SBMA, including changes in the sodium and chloride channels (6,19,44,57).

Synaptophysin staining is enhanced in both models

Confocal analysis revealed increased synaptophysin staining in the preterminal and terminal axon of diseased junctions suggesting an aberrant accumulation of synaptic vesicles. While preterminal axons were difficult to identify without serial reconstruction, we did not however find an increase in the density of vesicles in the nerve terminal at the ultrastructural level. This finding suggests that perhaps the increased synaptophysin staining in the nerve terminal reflects increased synaptophysin in the plasma membrane, where synaptophysin also resides as a result of exocytosis. The apparent accumulation of synaptophysin may be due to the impaired endocytosis that our endosomal trafficking data indicate (20). Because diseased terminals in both models release fewer vesicles in response to an action potential (19), enhanced exocytosis could not readily explain the accumulation of synaptophysin. We also acknowledge, however, that one cross section per junction may not offer sufficient power to detect at the ultrastructural level a difference in vesicular distribution within the nerve terminal.

Vesicular shape was affected in both models

While the size of vesicles was not affected, their shape was. Vesicles in both disease models were more ovoid than in WT controls. Changes in the shape of vesicles have been linked to changes in osmolarity and/or the content within vesicles (58,59) and whether the nerve terminal has been recently activated (60–63). Interestingly, quantal size is bigger at diseased junctions in both the myogenic TG and KI models (19), suggesting that the change in vesicular shape reported here may be related to higher concentrations of acetylcholine inside the vesicles. This difference may reflect an attempt to compensate for the impaired release of the vesicles. Regardless of why vesicles are less round than in WT terminals, the fact that both models show this same change in vesicular shape suggests it is a core feature of neuromuscular synapses affected by SBMA, and may shed light on the mechanisms affecting synaptic function in this disease.

Strategies for identifying core attributes of disease

We utilized two models that show comparable androgen-dependent motor dysfunction but have distinct differences in the underlying genetics that trigger disease. The aim of such cross-model comparisons is to identify core pathological traits that could explain the motor dysfunction characteristic of both models. The current study identified several common pathological indices of disease that likely represent the morphological substrates for synaptic dysfunction. 1) Quantal size is increased in the EDL of myogenic males and the LA of KI males (19), the same muscles examined here. The likely structural correlate for this change in quantal size is a change in vesicular shape. 2) Quantal content is also reduced in these same muscles, but involves different mechanisms. While both models show deficits in release probability, only myogenic synapses show decreases in RRP size (19). This is consistent with current findings that only myogenic mice show fewer docked vesicles. Deficits in release probability may precede deficits in the RRP since acutely diseased myogenic females also show comparable deficits in quantal release and strength without effects on RRP size (Xu and Jordan, unpublished observation). Hence, some differences in synaptic pathology across different models may be related to different stages of disease. While junctional fragmentation was also found in chronically diseased males of both models, this too may be a rather late event contributing to synaptic dysfunction since weak junctions in acutely diseased females are not fragmented (20). 3) It seems likely that the increased width of the primary cleft found in both models contributes to deficits in synaptic strength exhibited by both models. 4) The enhanced synaptophysin staining found in the TA muscle of both models suggest defects in the endocytotic pathway, as indicated by measures of endosomal transport (20). While other correlates of disease were found, including NF accumulation and changes in mitochondrial size, their role in synaptic dysfunction is less clear because they were present in one but not both models. In conclusion, by conducting cross-model comparisons, we begin to identify core defects that may critically mediate impairments in motor function in patients with SBMA. Because junctions are not denervated in chronically diseased mice in either model, it is unlikely that denervation triggers motor dysfunction in SBMA.

Methods

Spinal bulbar muscular atrophy mouse models

KI model. KI mice express a humanized AR containing the first exon of the human *AR* gene with an expanded number of CAG repeats from the endogenous AR mouse gene, as previously described (6). Because expression of the *AR* gene is controlled by endogenous promoters and enhancers, levels and patterns of mutant protein expression mimic those in WT mice. KI males and age-matched WT controls on a C57/B6J background were obtained from our breeding colony with a mean age of 183 days (± 15.92 SEM) for the confocal analysis and a mean age of 144 days (± 11.9 SEM) for the electron microscopic (EM) analysis. KI mice in both cohorts displayed comparable levels of dysfunction.

Myogenic model

TG mice in this model express a WT rat AR transgene exclusively in skeletal muscle fibres as described previously (Monks et al 2007). Transgenic females on a C57/B6J background were crossed with TG mice expressing YFP in motoneurons (Jackson Laboratories, stock number 003709), which allows detection of possible changes in neurofilament and synaptic vesicle distribution independent of the motor nerve terminal itself. Use of both YFP and synaptophysin for example allowed us to distinguish between *apparent* and actual denervation. It was possible that apparently denervated junctions based on synaptophysin staining might be structurally intact based on YFP. The previous characterization of such YFP-expressing mice established that expression of YFP transgene is not toxic to motor nerve terminals and has no apparent effect on their morphology (64). For the confocal analysis, we studied the adult male progeny of this cross—mice carrying the disease-causing AR allele or not (control) and the YFP allele (mean age = 212 days (± 13.06 SEM)).

Because many TG males in the myogenic model die at birth due to severely compromised motor function, subcutaneous flutamide injections (5mg/0.1ml propylene glycol) were given to pregnant dams on gestational days 15–20 to block androgen toxicity before birth, thus increasing the postnatal survival of TG males. Such flutamide-rescued TG males demonstrate the same androgen-dependent disease phenotype as those who did not receive prenatal flutamide (18). All TG and WT control males of the myogenic line that were used in these studies were exposed to flutamide prenatally. A second cohort of myogenic TG and WT males (mean age = 93-days-old (± 0.21 SEM) were similarly generated for the EM analysis but lacked the YFP gene.

Animals were group housed on a 12:12 light dark cycle with food and water provided *ad libitum*. Animals were weaned at 21 days and screened for either the expanded repeat region in exon I of the AR (for KIs) or the human skeletal α actin promoter (for myogenics) using PCR as previously described (6,17). All animal procedures were approved and performed in compliance with the Michigan State University Institutional Animal Care and Use Committee, in accordance with the standards in the NIH Guide for the Care and Use of Laboratory Animals.

Motor Function Measurements

Due to the predictable development of the motor phenotype in the myogenic model, animals were tested each of three days prior to muscle harvest with the mean of the three test days reported (Figure 1). In contrast, KI males show a large degree of

variability in the onset of motor deficits and were tested weekly starting at five weeks of age until they demonstrated a 70% deficit compared to WT controls in fore- and hindpaw grip strengths. Average motor function from the final testing week is reported (Figure 1).

Motor function was assessed based on measures of grip strength, and capacity to hang as previously described (9). The grid attachment was used to assess the grip strength of mice in both models. Male mice were held by the tail and lowered to a grid attached to a force gauge (Chatillon Force Measurement Systems, Largo FL), allowing either forepaws and/or hind paws to grasp the grid. They were pulled perpendicular to the grid with grip force recorded at the moment of release. This test was repeated six times in a single session, with the average of the four median values recorded as the grip strength score for that session and mouse. Grip strength in KI mice was also assessed using the triangle attachment as previously described (6,65), pulling the tail in the horizontal plane to assess grip strength at the moment of release. The grip strength score for that session was the mean of five scores. Mice in both models were also tested on the hang test. Mice were placed upright on a metal grid 40 cm above the bench top, which was subsequently slowly rotated 180 degrees. Latency to fall was measured up to a maximum of 120 s.

Light Microscopy Analysis of the NMJ

Immunocytochemistry

NMJs were stained in the perineal levator ani (LA) muscle of KI and WT males. The LA was chosen for study because ARs are normally highly expressed in this muscle compared to limb muscles, resulting in much more marked effects of the disease allele in the LA compared to limb musculature (6,44). The LA is also ideally suited for studying NMJs, given that it is a relatively flat muscle with a highly defined endplate band. However, we could not study the LA in the myogenic model because males in this model lacked this muscle. The LA requires prenatal androgens to survive and one result of exposing males to flutamide prenatally is that the LA is absent in such TG and WT males (66,67). Consequently, we selected a hindlimb muscle, the anterior tibialis (TA), another fast twitch muscle which does not require androgen exposure for its survival perinatally.

Muscles were harvested from male mice that were deeply anaesthetized with isoflurane. They were pinned flat as whole mounts in Sylgard-coated petri dishes, rinsed thoroughly with cold phosphate-buffered-saline (PBS, 0.14 M NaCl, 2.7 mM KCl, 1.5 mM KH_2PO_4 and 8 mM dibasic Na_2HPO_4 $7H_2O$, pH 7.4), fixed for 30 min in phosphate-buffered (0.1M, pH 7.4) 4% paraformaldehyde and cryoprotected in phosphate-buffered 20% sucrose for a minimum of three hours at room temperature. Muscles were longitudinally sectioned on a sliding, freezing microtome at 60 um, generating three series of sections, with each series stained to visualize the different cellular elements of the junction: synaptic vesicles, neurofilaments or tSCs. Postsynaptic acetylcholine receptors (AChRs) were visualized in all three series. Sections were collected and rinsed as free floating sections in a vehicle solution of PBS (constituents noted above) containing triton X-100 (0.3%), bovine serum albumin (0.2%) and sodium azide (0.1%) and incubated overnight at room temperature in the PBS vehicle containing primary antibody directed against one of the three elements of the junction. The following day, sections were rinsed and incubated for two hours in PBS vehicle containing fluorescently tagged secondary and α-bungarotoxin.

In the first series, synaptic vesicles were labelled using a rabbit anti-synaptophysin polyclonal primary (Zymed, 18-0130, diluted 1:50) and visualized with a sheep anti-rabbit Cy-3 labelled secondary (Sigma, C2306, diluted 1:100). In the second series, tSCs were labelled using rabbit anti-S100 polyclonal primary, a Schwann cell specific antigen (Dako, Z0311, diluted 1:400), and visualized with the same Cy-3 labelled secondary. The final series of sections was labelled using a mouse anti-neurofilament monoclonal antiserum (Developmental Studies Hybridoma Bank, 2H3 diluted 1:200) and visualized with a rabbit anti-mouse TRITC labelled secondary (Sigma, T2402, diluted 1:100). Acetylcholine receptors were labelled in all three series using AlexaFluor 647 conjugated alpha-bungarotoxin (Invitrogen, B35450, diluted 1:100). After several final rinses in PBS vehicle, muscle sections were mounted onto gel-subbed slides and allowed to dry in the dark for at least 24 hours. Slides were then dehydrated in graded ethanols, cleared in Hemo-De, and coverslipped using DPX, a non-fluorescing coverslipping medium. All fluorescently labelled material was stored at −20 °C after the DPX had set.

Confocal Imaging

A Zeiss LSM 510 Meta Confocal Microscope (Carl Zeiss, Oberkochen Germany) at the Center for Advanced Microscopy at Michigan State University (www.ceo.msu.edu, date last accessed July 20, 2016) was used to image pre- and post-synaptic specialization of individual NMJs. Areas of interest were first located using epifluorescent illumination beginning at one margin of a muscle section and systematically working along the endplate band. Only junctions that were *en face* were imaged. Images were scanned using an Olympus 63× 1.4 NA oil objective, without digital zoom. The confocal pinhole aperture was set to 1.11 Airy disk, with the image size set at 1024×1024 pixels and the Z-step size set at 0.9μm. For each junction, a stack of images was collected through the entire depth containing visible signal. Lasers at 488, 543 and 633 nm were used in sequential mode to visualize different components of the same junction. Each of the channels was visualized independently to confirm that there was no channel crossover. For each series and labels, channel settings were optimized and then held constant for the following parameters: laser power, detector gain, amplifier gain, pinhole and offset. Image processing was completed using Zeiss LSM Image Browser.

Confocal Image Analysis

All analyses were conducted by an observer 'blind' to the animals' group membership. Twenty *en face* junctions were imaged for each animal of each series. Images of NMJs were constructed by projecting through the Z-axis planes and using the most intense pixels to create a composite image of a junction showing staining for synaptophysin, neurofilament or tSCs presynaptically, with the endplate marked for each by AChR. Once junctions were constructed, such images were analysed. The YFP signal was systematically monitored in the synaptophysin series and revealed that YFP and synaptophysin staining consistently colocalized throughout the nerve terminal. That is, we never encountered a nerve terminal where portions were marked by YFP staining but lacked synaptophysin staining, indicating that synaptophysin staining reliably reflected the structure of the nerve terminal itself. Nonetheless, it is important to point out that while synaptophysin staining aligned well with both the YFP label and AChR staining, synaptophysin staining was not

uniformly dense throughout the terminal, resulting in about 40% coverage of the endplate in normal muscle when the image was thresholded. Given that synaptic vesicles occupy only about 4% of the overall volume of a mouse NMJ (68), we were not surprised by our estimates of ~40% coverage for WT junctions based on synaptophysin staining.

Synaptophysin/AChR-labelled series

We took five measures in this series. The size of junctions was measured based on the area occupied by stained postsynaptic AChRs (1), and based on the area occupied by presynaptic synaptophysin staining (2). Given the precise alignment of pre- and post-synaptic elements typical of normal NMJs, such pre- and post-synaptic measures were expected to yield comparable estimates of endplate area in WT muscle. However, the disease commonly disrupts this relationship, with estimates of junctional size based on endplate area (AChR staining) larger than estimates based on presynaptic elements (synaptophysin staining). Such a result would suggest junctions are denervated. A change in the other direction would suggest nerve terminal sprouting and/or an accumulation of synaptic vesicles in motor nerve terminals. We also assessed directly whether junctions were denervated (3) using overlays of synaptophysin/AChR stained junctions; partial or full denervation was indicated by the presence of exposed postsynaptic AChR staining which lacked overlying nerve terminal. Junctional fragmentation was also assessed in this series based on AChR staining, with a fully connected pretzel-like pattern of receptor labelling taken as evidence of no fragmentation, partially disconnected AChR-rich domains indicating partial fragmentation or completely disconnected clusters of grape-like domains indicating complete fragmentation. In reality, these apparently separate clusters of innervation were connected via fine processes that could only be detected at the EM level. Such fine processes neither contained synaptic vesicles nor were in contact with post-synaptic specializations suggesting that such fine inter-connectives were used for electrical conduction but did not themselves release neurotransmitter.

To assess the area occupied by either synaptophysin or AChR staining, images were exported from the Zeiss LSM Image Browser, cropped in Adobe Photoshop CS5, subjected to unsharp mask filter (parameters set to amount:500, radius:50, and threshold:1) and thresholded. When thresholding, the grey values of the unsharp mask image were adjusted to the best fit of the original image. Thresholded images were re-opened in ImageJ and the number-of-pixels function was used to estimate the junctional area (4) from corresponding thresholded images of presynaptic and postsynaptic staining of individual junctions. Such estimates were used to determine the percent of synaptophysin staining covering the endplate. ImageJ was also used to measure the width of muscle fibres (5) at the middle of the junctions in the max projection images from the synaptophysin-labelled series.

Neurofilament/AChR stained series

We took three measures in this series. We counted the number of neurofilament accumulations in the terminal (1) and in the preterminal axon (2). Neurofilament accumulations in the nerve terminal were defined as neurofilament-positive bulbous swellings of at least twice the diameter of the rest of the neurofilament-stained terminal branches and colocalized with AChR labelled endplate. Neurofilament accumulations in the axon were defined as localized neurofilament-positive bulbous

swellings located in the myelinated axon, proximal to the pre-terminal branch that were of at least twice the overall caliber of the axon. The number of terminal sprouts (3) were also counted. Nerve terminal sprouts were defined as fine, neurofilament-labelled processes extending beyond the perimeter of the junction (marked by AChR staining) of no less than 15 microns and having blunt, bulbous endings in contrast to the thin tapered ends of terminal branches. Such processes were not associated with AChR labelling.

tSC/AChR labelled series

We counted the number of tSCs capping the junction based on the number of round, slightly transparent nuclei surrounded by a rim of increased density S100 staining overlying postsynaptic AChR labelling. The morphology of tSCs was also assessed by counting the number of tSCs sprouts, defined as fine processes extending no less than 15μm beyond the outer perimeter of the endplate as marked by AChR staining.

EM Analysis of NMJ Morphology

Fixation

A separate cohort of animals were generated for the EM analysis of NMJs that achieved comparable levels of motor dysfunction as the first cohort (Figure 1). The LA in the KI model and the EDL in the myogenic model were harvested from male mice deeply anaesthetized with isofluorane. We switched to the smaller EDL because the considerably larger TA muscle resulted in uneven fixation and artefacts in ultrastructure. Muscles were pinned under tension in Sylgard-coated dishes, cleaned, and allowed to recover at room temperature for 5–30 min in oxygenated Ringer's (135 mM NaCl, 5 mM KCl, 2 mM $CaCl_2$, 1 mM $MgCl_2$, 14 mM Hepes buffer, 11 mM dextrose, pH 7.4). Muscles were then incubated 2–7 min in cold oxygenated Ringer's in which the $CaCl_2$ was replaced by equimolar amounts of $MgCl_2$. Muscles were then fixed using a cold aldehyde fixative (4% paraformaldehyde, 1% glutaraldehyde, in 0.1 M Millonig's phosphate buffer, pH 7.2) for 2–2.5 hours at 4°C. After ≥ 30 min of fixation, small pieces of the endplate region of the muscle were dissected and placed in vials of fresh fixative. After aldehyde fixation, the muscle pieces were rinsed six times in Millonig's buffer (pH 7.2) and left overnight at 4°C. Samples were postfixed in 1% OsO_4 in 0.1M Millonig's phosphate buffer for two hours, rinsed in buffer, and then dehydrated in a graded series of ethanols and propylene oxide. They were then infiltrated in a graded series of propylene oxide/Araldite 502 resin mixtures to 100% resin over a period of 24 hours. The pieces of muscle were flat embedded in aluminium dishes and the resin was cured at 60°C under vacuum for three days.

Sectioning and Imaging

Blocks were thick-sectioned perpendicular to the long axis of the muscle fibres until junctions could be identified at which point ultrathin sections were taken. Thin sections were stained with 10% uranyl acetate in 50% methanol and Reynold's lead citrate. The last thick section cut prior to taking thin sections was photographed with a light microscope, and individual junctions were identified and numbered. Every junction identified in the block face was photographed in thin sections using the electron microscope (JEOL 100CX, Michigan State University Center for Advanced Microscopy) at 80kV at three magnifications. Each junction was first imaged using a lower magnification to provide contextual information about the profile, an intermediate and

high magnification. All measurements were taken with high magnification images (approximately 20,000×) which provided the requisite resolution. Exact magnifications were determined by photographing a calibration grating of 2160 lines/mm. Plastic negatives (3.25" × 4") were developed and scanned with an Epson Perfection V750 Pro scanner at 600 dpi and the resulting files saved for analysis without enhancement.

EM Image Analysis

One of multiple images from the same junction that showed clear postsynaptic folds, a recognizable nerve terminal and tSCs was randomly chosen for quantitative analysis. Ten different junctions per animal were sampled. Digitized images were opened in Adobe Photoshop and precisely aligned to reconstruct a junction if the profile filled more than one view frame. Using the Photoshop Layers feature, numerous layers were superimposed upon the original image, and each layer was used to trace, count, or measure various features of the terminal profile and exported from Photoshop as individual files. Layers that required area, length or number measurements were reopened in FIJI (69), a mask was created, and then measurements were taken, with Particle Count applied for estimating number of objects. Layers featuring non-straight lines were opened in Adobe Illustrator and Live Trace was used with a threshold of 184 to produce a continuous stroke from which the continuous path length could be read.

Presynaptic measures

Measured presynaptic features included the area of the membrane bound terminal profile. Within this profile, we also measured the number and cross sectional area of mitochondria. The overall number of vesicles were also counted as well as vesicles in the synaptic zone, defined as a 480 nm wide strip of terminal directly across from the synaptic cleft. This measure was aimed at estimating the number of vesicles in the RRP. Vesicle diameter was also measured from this subset of vesicles by taking the horizontal and vertical diameter from the centre of each vesicle. The aspect ratio of the horizontal and vertical diameter of each vesicle was used as a measure of vesicle roundness.

Postsynaptic measures

We also extensively measured features of the primary and secondary synaptic clefts, including the total area and width of the primary synaptic cleft, and the number, area, width and depth of secondary clefts. Secondary clefts were defined as having a depth (peak to trough) of at least 104.5 nm. Total perimeter length of the postsynaptic folds and perimeter length of each secondary cleft was also measured. The number of active zones appearing as electron dense regions directly across from secondary clefts was counted and classified as having either docked vesicles (in contact with the presynaptic membrane) or not. Each measured feature of the post-synapse was divided by total apposition length of the terminal, to control for differences in size of junction in view. When the same feature (e.g., secondary cleft depth) was measured multiple times at the same junction, these values were averaged together to give a single estimate of that measure for that junction.

In addition to the numerous quantitative measures, junctions were qualitatively evaluated, noting evidence of anomalous features that might indicate disease-related changes. All analysis was conducted blind to group membership.

Statistical Analysis

Independent *t*-tests were run on each measure to determine whether statistically significant differences between disease and age matched WT control groups. Results are presented as group means (*n* = number of animals/group for the light microscope analysis and junction/group for the EM analysis) ± standard error of the mean.

Supplementary Material

Supplementary Material is available at *HMG* online.

References

1. Kariya, S., Park, G.H., Maeno-Hikichi, Y., Leykekhman, O., Lutz, C., Arkovitz, M.S., Landmesser, L.T. and Monani, U.R. (2008) Reduced SMN protein impairs maturation of the neuromuscular junctions in mouse models of spinal muscular atrophy. *Hum. Mol. Genet.*, **17**, 2552–2569.
2. Fischer, L.R., Culver, D.G., Tennant, P., Davis, A.A., Wang, M., Castellano-Sanchez, A., Khan, J., Polak, M.A. and Glass, J.D. (2004) Amyotrophic lateral sclerosis is a distal axonopathy: evidence in mice and man. *Experiment. Neurol.*, **185**, 232–240.
3. Yoshikawa, M., Vinsant, S., Mansfield, C.M., Moreno, R.J., Giffondorwa, D.J., Pace, L., Leles, B., Messi, L.M., Caress, J., Cartwright, M., *et al.* (2009) Identification of changes in muscle, neuromuscular junctions and spinal cord at early presymptomatic stages in mutant SOD1 mouse model of ALS may provide novel insight for diagnosis and treatment development. *Soc. Neurosci.* 2009, in press.
4. Frey, D., Schneider, C., Xu, L., Borg, J., Spooren, W. and Caroni, P. (2000) Early and selective loss of neuromuscular synapse subtypes with low sprouting competence in motoneuron diseases. *J. Neurosc.*, **20**, 2534–2542.
5. Balice-Gordon, R.J., Smith, D.B., Goldman, J., Cork, L.C., Shirley, A., Cope, T.C. and Pinter, M.J. (2000) Functional motor unit failure precedes neuromuscular degeneration in canine motor neuron disease. *Ann. Neurol.*, **47**, 596–605.
6. Yu, Z., Dadgar, N., Albertelli, M., Gruis, K., Jordan, C., Robins, D.M. and Lieberman, A.P. (2006) Androgen-dependent pathology demonstrates myopathic contribution to the Kennedy disease phenotype in a mouse knock-in model. *J. Clin. Invest.*, **116**, 2663–2672.
7. Katsuno, M., Adachi, H., Minamiyama, M., Waza, M., Tokui, K., Banno, H., Suzuki, K., Onoda, Y., Tanaka, F., Doyu, M., *et al.* (2006) Reversible disruption of dynactin 1-mediated retrograde axonal transport in polyglutamine-induced motor neuron degeneration. *J. Neurosci.*, **26**, 12106–12117.
8. Fischbeck, K.H., Souders, D. and La Spada, A. (1991) A candidate gene for X-linked spinal muscular atrophy. *Adv. Neurol.*, **56**, 209–213.

9. Johansen, J.A., Yu, Z., Mo, K., Monks, D.A., Lieberman, A.P., Breedlove, S.M. and Jordan, C.L. (2009) Recovery of function in a myogenic mouse model of spinal bulbar muscular atrophy. *Neurobiol. Dis.*, **34**, 113–120.

10. Katsuno, M., Adachi, H., Kume, A., Li, M., Nakagomi, Y., Niwa, H., Sang, C., Kobayashi, Y., Doyu, M. and Sobue, G. (2002) Testosterone reduction prevents phenotypic expression in a transgenic mouse model of spinal and bulbar muscular atrophy. *Neuron*, **35**, 843–854.

11. Kinirons, P. and Rouleau, G.A. (2008) Administration of testosterone results in reversible deterioration in Kennedy's disease. *J. Neurol. Neurosurg. Psychiat.*, **79**, 106–107.

12. Sobue, G., Hashizume, Y., Mukai, E., Hirayama, M., Mitsuma, T. and Takahashi, A. (1989) X-linked recessive bulbospinal neuronopathy. A clinicopathological study. *Brain*, **112 (Pt 1)**, 209–232.

13. Kennedy, W.R., Alter, M. and Sung, J.H. (1968) Progressive proximal spinal and bulbar muscular atrophy of late onset. A sex-linked recessive trait. *Neurology*, **18**, 671–680.

14. Cifuentes-Diaz, C., Nicole, S., Velasco, M.E., Borra-Cebrian, C., Panozzo, C., Frugier, T., Millet, G., Roblot, N., Joshi, V. and Melki, J. (2002) Neurofilament accumulation at the motor endplate and lack of axonal sprouting in a spinal muscular atrophy mouse model. *Hum. Mol. Genet.*, **11**, 1439–1447.

15. Lin, T.L., Chen, T.H., Hsu, Y.Y., Cheng, Y.H., Juang, B.T. and Jong, Y.J. (2016) Selective Neuromuscular Denervation in Taiwanese Severe SMA Mouse Can Be Reversed by Morpholino Antisense Oligonucleotides. *PloS One*, **11**, e0154723.

16. Ling, K.K., Gibbs, R.M., Feng, Z. and Ko, C.P. (2012) Severe neuromuscular denervation of clinically relevant muscles in a mouse model of spinal muscular atrophy. *Hum. Mol. Genet.*, **21**, 185–195.

17. Monks, D.A., Johansen, J.A., Mo, K., Rao, P., Eagleson, B., Yu, Z., Lieberman, A.P., Breedlove, S.M. and Jordan, C.L. (2007) Overexpression of wild-type androgen receptor in muscle recapitulates polyglutamine disease. *Proc. Natl Acad Sci. USA*, **104**, 18259–18264.

18. Johansen, J.A., Troxell-Smith, S.M., Yu, Z., Mo, K., Monks, D.A., Lieberman, A.P., Breedlove, S.M. and Jordan, C.L. (2011) Prenatal flutamide enhances survival in a myogenic mouse model of spinal bulbar muscular atrophy. *Neurodegener Dis.*, **8**:25–34.

19. Xu, Y., Halievski, K., Henley, C., Atchison, W.D., Katsuno, M., Adachi, H., Sobue, G., Breedlove, S.M. and Jordan, C.L. (2016) Defects in neuromuscular transmission may underlie motor dysfunction in spinal and bulbar muscular atrophy. *J. Neurosci.*, **36**, 5094–5106.

20. Kemp, M.Q., Poort, J.L., Baqri, R.M., Lieberman, A.P., Breedlove, S.M., Miller, K.E. and Jordan, C.L. (2011) Impaired motoneuronal retrograde transport in two models of SBMA implicates two sites of androgen action. *Hum. Mol. Genet.*, **20**, 4475–4490.

21. Lubischer, J.L. and Bebinger, D.M. (1999) Regulation of terminal Schwann cell number at the adult neuromuscular junction. *J. Neurosci.*, **19**, RC46.

22. Slater, C.R., Fawcett, P.R.W., Walls, T.J., Lyons, P.R., Bailey, S.J., Beeson, D., Young, C. and Gardner-Medwin, D. (2006) Pre- and post-synaptic abnormalities associated with impaired neuromuscular transmission in a group of patients with 'limb-girdle myasthenia'. *Brain*, **129**, 2061–2076.

23. Deconinck, A.E., Rafael, J.A., Skinner, J.A., Brown, S.C., Potter, A.C., Metzinger, L., Watt, D.J., Dickson, J.G., Tinsley, J.M. and Davies, K.E. (1997) Utrophin-dystrophin-deficient mice as a model for Duchenne muscular dystrophy. *Cell*, **90**, 717–727.

24. Banks, G.B., Chamberlain, J.S. and Froehner, S.C. (2009) Truncated dystrophins can influence neuromuscular synapse structure. *Mol. Cell. Neurosci.*, **40**, 433–441.

25. Kong, J. and Anderson, J.E. (1999) Dystrophin is required for organizing large acetylcholine receptor aggregates. *Brain Res.*, **839**, 298–304.

26. Lyons, P.R. and Slater, C.R. (1991) Structure and function of the neuromuscular junction in young adult mdx mice. *J. Neurocytol.*, **20**, 969–981.

27. Torres, L.F. and Duchen, L.W. (1987) The mutant mdx: inherited myopathy in the mouse. Morphological studies of nerves, muscles and end-plates. *Brain*, **110 (Pt 2)**, 269–299.

28. Love, F.M. and Thompson, W.J. (1999) Glial cells promote muscle reinnervation by responding to activity-dependent postsynaptic signals. *J. Neurosci.*, **19**, 10390–10396.

29. Son, Y.J. and Thompson, W.J. (1995) Nerve sprouting in muscle is induced and guided by processes extended by Schwann cells. *Neuron*, **14**, 133–141.

30. Brown, M.C., Holland, R.L. and Ironton, R. (1980) Nodal and terminal sprouting from motor nerves in fast and slow muscles of the mouse. *J. Physiol.*, **306**, 493–510.

31. Gundersen, K., Sanes, J.R. and Merlie, J.P. (1993) Neural regulation of muscle acetylcholine receptor epsilon- and alpha-subunit gene promoters in transgenic mice. *J. Cell Biol.*, **123**, 1535–1544.

32. Ziskind-Conhaim, L. and Bennett, J.I. (1982) The effects of electrical inactivity and denervation on the distribution of acetylcholine receptors in developing rat muscle. *Dev.Biol.*, **90**, 185–197.

33. Chevalier-Larsen, E.S., Wallace, K.E., Pennise, C.R. and Holzbaur, E.L. (2008) Lysosomal proliferation and distal degeneration in motor neurons expressing the G59S mutation in the p150Glued subunit of dynactin. *Hum. Mol. Genet.*, **17**, 1946–1955.

34. Shiao, T., Fond, A., Deng, B., Wehling, H.M., Adams, M.E., Froehner, S.C. and Tidball, J.G., (2004) Defects in neuromuscular junction structure in dystrophic muscle are corrected by expression of a NOS transgene in dystrophin-deficient muscles, but not in muscles lacking alpha- and beta1-syntrophins. *Hum. Mol. Genet.*, **13**, 1873–1884.

35. Pratt, S.J., Shah, S.B., Ward, C.W., Inacio, M.P., Stains, J.P. and Lovering, R.M. (2013) Effects of in vivo injury on the neuromuscular junction in healthy and dystrophic muscles. *J. Physiol.*, **591**, 559–570.

36. Grady, R.M., Teng, H., Nichol, M.C., Cunningham, J.C., Wilkinson, R.S. and Sanes, J.R. (1997) Skeletal and cardiac myopathies in mice lacking utrophin and dystrophin: a model for Duchenne muscular dystrophy. *Cell*, **90**, 729–738.

37. Kulakowski, S.A., Parker, S.D. and Personius, K.E. (2011) Reduced TrkB expression results in precocious age-like changes in neuromuscular structure, neurotransmission, and muscle function. *J. Appl. Physiol. (1985)*, **111**, 844–852.

38. Li, Y., Lee, Y. and Thompson, W.J. (2011) Changes in aging mouse neuromuscular junctions are explained by degeneration and regeneration of muscle fiber segments at the synapse. *J. Neurosci.*, **31**, 14910–14919.

39. Cortes, C.J., Ling, S.C., Guo, L.T., Hung, G., Tsunemi, T., Ly, L., Tokunaga, S., Lopez, E., Sopher, B.L., Bennett, C.F., *et al.* (2014) Muscle expression of mutant androgen receptor accounts for systemic and motor neuron disease phenotypes in spinal and bulbar muscular atrophy. *Neuron*, **82**, 295–307.

40. Butikofer, L., Zurlinden, A., Bolliger, M.F., Kunz, B. and Sonderegger, P. (2011) Destabilization of the neuromuscular junction by proteolytic cleavage of agrin results in precocious sarcopenia. *FASEB J.*, **25**, 4378–4393.

41. Lee, Y.I., Li, Y., Mikesh, M., Smith, I., Nave, K.A., Schwab, M.H. and Thompson, W.J. (2016) Neuregulin1 displayed on motor axons regulates terminal Schwann cell-mediated synapse elimination at developing neuromuscular junctions. *Proc. Natl Acad. Sci. USA*, **113**, E479–E487.

42. Gonzalez, M., Ruggiero, F.P., Chang, Q., Shi, Y.J., Rich, M.M., Kraner, S. and Balice-Gordon, R.J. (1999) Disruption of Trkb-mediated signaling induces disassembly of postsynaptic receptor clusters at neuromuscular junctions. *Neuron*, **24**, 567–583.

43. Halievski, K., Henley, C.L., Domino, L., Poort, J.E., Fu, M., Katsuno, M., Adachi, H., Sobue, G., Breedlove, S.M. and Jordan, C.L. (2015) Androgen-dependent loss of muscle BDNF mRNA in two mouse models of SBMA. *Exp. Neurol.*, **269**, 224–232.

44. Yu, Z., Wang, A.M., Robins, D.M. and Lieberman, A.P. (2009) Altered RNA splicing contributes to skeletal muscle pathology in Kennedy disease knock-in mice. *Dis. Model Mech.*, **2**, 500–507.

45. Jirmanova, I. (1975) Ultrastructure of motor end-plates during pharmacologically-induced degeneration and subsequent regeneration of skeletal muscle. *J. Neurocytol.*, **4**, 141–155.

46. Miledi, R. and Slater, C.R. (1970) On the degeneration of rat neuromuscular junctions after nerve section. *J. Physiol.*, **207**, 507–528.

47. Jordan, C.L., Letinsky, M.S. and Arnold, A.P. (1989) The role of gonadal hormones in neuromuscular synapse elimination in rats. I. Androgen delays the loss of multiple innervation in the levator ani muscle. *J. Neurosci.*, **9**, 229–238.

48. Jordan, C.L., Letinsky, M.S. and Arnold, A.P. (1989) The role of gonadal hormones in neuromuscular synapse elimination in rats. II. Multiple innervation persists in the adult levator ani muscle after juvenile androgen treatment. *J. Neurosci.*, **9**, 239–247.

49. Renger, J.J., Egles, C. and Liu, G. (2001) A developmental switch in neurotransmitter flux enhances synaptic efficacy by affecting AMPA receptor activation. *Neuron*, **29**, 469–484.

50. Law, P.K., Saito, A. and Fleischer, S. (1983) Ultrastructural changes in muscle and motor end-plate of the dystrophic mouse. *Exp. Neurol.*, **80**, 361–382.

51. Engel, A.G. and Santa, T. (1971) Histometric analysis of the ultrastructure of the neuromuscular junction in myasthenia gravis and in the myasthenic syndrome. *Ann. N Y. Acad. Sci.*, **183**, 46–63.

52. Conti-Fine, B.M., Milani, M. and Kaminski, H.J. (2006) Myasthenia gravis: past, present, and future. *J. Clin. Invest.*, **116**, 2843–2854.

53. Wairkar, Y.P., Fradkin, L.G., Noordermeer, J.N. and DiAntonio, A. (2008) Synaptic defects in a Drosophila model of congenital muscular dystrophy. *J. Neurosci.*, **28**, 3781–3789.

54. Savtchenko, L.P. and Rusakov, D.A. (2007) The optimal height of the synaptic cleft. *Proc. Natl Acad. Sci. U S A*, **104**, 1823–1828.

55. Bailey, S.J., Stocksley, M.A., Buckel, A., Young, C. and Slater, C.R. (2003) Voltage-gated sodium channels and ankyrinG occupy a different postsynaptic domain from acetylcholine receptors from an early stage of neuromuscular junction maturation in rats. *J. Neurosci.*, **23**, 2102–2111.

56. Flucher, B.E. and Daniels, M.P. (1989) Distribution of Na+ channels and ankyrin in neuromuscular junctions is complementary to that of acetylcholine receptors and the 43 kd protein. *Neuron*, **3**, 163–175.

57. Oki, K., Halievski, K., Vicente, L., Xu, Y., Zeolla, D., Poort, J., Katsuno, M., Adachi, H., Sobue, G., Wiseman, R.W., *et al.* (2015) Contractile dysfunction in muscle may underlie androgen-dependent motor dysfunction in spinal bulbar muscular atrophy. *J. Appl. Physiol.*, **118**, 941–952.

58. Thureson-Klein, A., Klein, R.L. and Chen Yen, S.H. (1975) Morphological effects of osmolarity on purified noradrenergic vesicles. *J. Neurocytol.*, **4**, 609–627.

59. Langmeier, M., Giogasova, E., Zikova, O. and Mares, J. (1986) Changes in the size and shape of the synaptic vesicles in the sensorimotor cortex of the rat brain in the initial phases of kindling. *Physiol. Bohemoslov.*, **35**, 437–446.

60. Jones, S.F. and Kwanbunbumpen, S. (1970) Some effects of nerve stimulation andhemicholinium on quantal transmitter release at the mammalian neuromuscular junction. *J. Physiol.*, **207**, 51–61.

61. Korneliussen, H. (1972) Ultrastructure of normal and stimulated motor endplates with comments on the origin and fate of synaptic vesicles. *Z. Zellforsch. Mikrosk. Anat.*, **130**, 28–57.

62. Heuser, J.E. and Reese, T.S. (1973) Evidence for recycling of synaptic vesicle membrane during transmitter release at the frog neuromuscular junction. *J. Cell Biol.*, **57**, 315–344.

63. Pysh, J.J. and Wiley, R.G. (1974) Synaptic vesicle depletion and recovery in cat sympathetic ganglia electrically stimulated in vivo. Evidence for transmitter secretion by exocytosis. *J. Cell Biol.*, **60**, 365–374.

64. Feng, G., Mellor, R.H., Bernstein, M., Keller-Peck, C., Nguyen, Q.T., Wallace, M., Nerbonne, J.M., Lichtman, J.W. and Sanes, J.R. (2000) Imaging neuronal subsets in transgenic mice expressing multiple spectral variants of GFP. *Neuron*, **28**, 41–51.

65. Kemp, M., Poort, J., Baqri, R., Breedlove, S. and Miller, K., Miller, KC.L.J., (2009) Live imaging of endosomal trafficking deficits in sciatic nerves of a myogenic mouse model of SBMA. *Soc. Neurosci.*, in press.

66. Breedlove, S.M. and Arnold, A.P. (1983) Hormonal control of a developing neuromuscular system. I. Complete Demasculinization of the male rat spinal nucleus of the bulbocavernosus using the anti-androgen flutamide. *J. Neurosci.*, **3**, 417–423.

67. Sengelaub, D.R., Nordeen, E.J., Nordeen, K.W. and Arnold, A.P. (1989) Hormonal control of neuron number in sexually dimorphic spinal nuclei of the rat: III. Differential effects of the androgen dihydrotestosterone. *J. Comp. Neurol.*, **280**, 637–644.

68. Wilhelm, B.G., Mandad, S., Truckenbrodt, S., Krohnert, K., Schafer, C., Rammner, B., Koo, S.J., Classen, G.A., Krauss, M., Haucke, V., *et al.* (2014) Composition of isolated synaptic boutons reveals the amounts of vesicle trafficking proteins. *Science*, **344**, 1023–1028.

69. Schindelin, J., Arganda-Carreras, I., Frise, E., Kaynig, V., Longair, M., Pietzsch, T., Preibisch, S., Rueden, C., Saalfeld, S., Schmid, B., *et al.* (2012) Fiji: an open-source platform for biological-image analysis. *Nat. Met.*, **9**, 676–682.